ACS APPLIED MATERIALS & INTERFACES

www.acsami.org

Research Article

Preferred Film Orientation to Achieve Stable and Efficient Sn−Pb Binary Perovskite Solar Cells

Yansen Sun, Shuo Yang, Zhenyu Pang, Yingnan Quan, Rongfei Song, Yu Chen, Weiheng Qi, Yanbo Gao, Fengyou Wang, Xinyuan Zhang, Yunfei Sun, Jinghai Yang,* Lili Yang,* and Federico Rosei*

Cite This: *ACS Appl. Mater. Interfaces* 2021, 13, 10822−10836

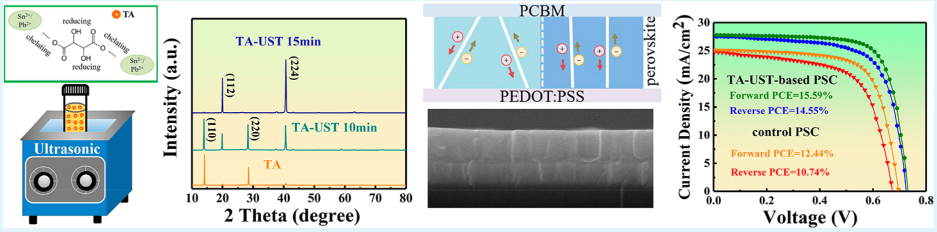

ABSTRACT: The preferred orientation of crystalline films in hybrid perovskite materials is known to influence the performance of perovskite solar cells (PSCs). Although the preferred growth along the (112) directions has been reported to promote charge transport within the Pb-based polycrystalline perovskite films, the preferred orientation growth of this facet is still difficult to be achieved due to the higher formation energy compared with the (110) plane. Herein, Sn−Pb binary perovskite films with a well-controlled orientation along the (224) plane were achieved by introducing a simple ultrasonic treatment (UST) into the additive engineering fabricated method. UST is used to process the perovskite precursor solutions of tartaric acid (TA) modified Sn−Pb binary polycrystalline perovskite films to regulate the interactions between PbI_2/SnI_2 and TA in the intermediate phases. Meanwhile, TA-modulated $MA_{0.9}Cs_{0.1}Pb_{0.75}Sn_{0.25}I_3$-based perovskite films with a preferred orientation of (224) crystal plane were obtained by precisely controlling the UST time to 15 min. The highest power conversion efficiency (PCE) of 15.59% with less hysteresis and improved stability was achieved, while realizing 8.64 and 25.32% enhancements of PCE compared with that of TA-based and control counterparts with (110) preferred orientation, respectively. Our work provides a promising route to obtain preferred orientation growth of polycrystalline perovskite films. In particular, we have shown that this approach improves the performance of Sn−Pb binary PSCs, while such methodology is quite flexible and could also be applied to other low-/non-toxic PSCs.

KEYWORDS: *Sn−Pb binary perovskite, preferred orientation growth, tartaric acid, ultrasonic treatment, photovoltaic performance*

■ INTRODUCTION

Addressing the energy challenges and related climate changes relies on the urgent development and deployment of high-performance renewable energy technologies, wherein the third-generation photovoltaic (PV) devices are considered particularly promising due to the relative abundance of solar irradiation on the earth's surface.[1] In this context, three-dimensional (3D) hybrid organic−inorganic halide perovskite solar cells (PSCs) (AMX_3, A = Cs^+/$CH_3NH_3^+$/NH = $CHNH_3^+$; M = Pb^{2+}/Sn^{2+}; X = Cl^-/Br^- and I^-) have been extensively studied since their first demonstration due to the increasing power conversion efficiency (PCE).[2−7] Nevertheless, several challenges still need to be addressed before PSCs can be commercialized. Although the PCE of state-of-the-art PSCs has been as high as 25.2%,[3] instability factors caused by light, heat, water, and the use of toxic elements (Pb) still hinder their large-scale application.[8,9]

Numerous strategies have been developed to improve the device performance, often by modulating the growth of perovskite films to optimize the optoelectronic properties. In particular, it was shown that the PV parameters of PSCs, including PCE, open-circuit voltage (V_{oc}), short-circuit photocurrent density (J_{sc}), and fill factor (FF) exhibit dependence on polycrystalline perovskite films grown with different preferred orientations of crystal planes.[10] Moreover, recent work has demonstrated the feasibility of controlling the preferred orientation growth of Pb-based perovskite films in different crystal planes.[11] For example, the controllable orientation of perovskite films can be achieved by cascading the A-site of $APbX_3$ hybrid perovskite polycrystalline films, which has been shown to facilitate the regulation of the charge transport properties.[12] Moreover, Liu et al. achieved preferential growth

Received: October 23, 2020
Accepted: February 11, 2021
Published: February 25, 2021

https://dx.doi.org/10.1021/acsami.0c19014
ACS Appl. Mater. Interfaces 2021, 13, 10822−10836

of the (224) facet by regulating the concentration of methylammonium acetate, which increased the grain size and enhanced the light absorption of $MAPbI_3$-based PSCs.[13] These results suggested that preferential orientation growth of perovskite films along different crystal planes can be realized by adjusting the synthesis conditions and controlling the intermediate phases, which will benefit the device performance of PSCs.[14,15]

However, it remains a challenge for controlling the nucleation orientation when adopting the conventional one-step spin-coating method, as the nature of hybrid perovskites can lead to extremely fast crystallization during film formation process.[16] Meanwhile, it is almost impossible to achieve the modulation of preferential orientation growth on different crystal planes in controllable manners for polycrystalline perovskite films without additional treatment, especially for lead-free or low-toxicity binary perovskites. Until now, Sn−Pb binary PSCs are still considered to be the most promising candidates for reducing device toxicity problems due to the suitable band gaps and high carrier mobility of these absorber layers.[17−20] However, the poor crystal qualities of the corresponding perovskite films still limit the enhancement of device performance and stability, mainly including the inferior chemical stability of Sn^{2+} in the perovskite crystal structure, which is easily oxidized to Sn^{4+}, and the fast crystallization rate among solutes.[21,22] In this context, the introduction of functional additives into perovskite precursor solutions has been demonstrated to further stabilize the perovskite crystal structure and improve the quality of Sn−Pb binary perovskite films by regulating the state of intermediate phases to retard the oxidation process of Sn^{2+} and to reduce the tin vacancies.[23,24] Although the PCE of Sn−Pb binary PSCs has reached more than 18%, the performance is still far below the record values of 25.2% for $MAPbI_3$-based devices.[25] Inspired by the positive effects of preferential orientation growth on $MAPbI_3$-based perovskite films, we aim to further improve the device performance of Sn−Pb binary PSCs by achieving the preferential growth of the corresponding perovskite films.

When adopting the one-step spin-coating method, the state of perovskite precursor solutions and the crystallization dynamics during the film formation process are two key factors affecting the quality of perovskite films. However, it is difficult to effectively control the crystallization process due to the fast crystallization rate between MAI and SnI_2 of Sn−Pb binary perovskite films. Therefore, controlling the state of perovskite precursor solutions by modulating the intermediate phases may be a promising approach for achieving preferential orientation growth of perovskite films. Hirsekorn revealed that polycrystalline materials are all made up of discrete grains and they all have regular crystalline atomic structures, but their crystallographic axes show different orientations due to the anisotropic elastic properties of the grains.[26] Moreover, Gielen et al. indicated that ultrasonic treatment (UST) can affect the crystal growth dynamics of different materials.[27] Therefore, we introduced this technique and acted on Sn−Pb binary perovskite precursor solutions to further regulate the interactions among solutes for the purpose of controlling the preferred orientation of the intermediate phase and perovskite films, especially after introducing extra Lewis bases of tartaric acid (TA) into them. Since the chelation greatly affects the orientation of PbI_2/SnI_2 crystal nucleation, the homogeneous distribution of TA after UST will further influence the chelation and eventually change the preferred orientation of perovskite films.[27,28]

Herein, the preparation of Sn−Pb binary perovskite films with preferred orientation along the (224) plane by combining the additive TA and UST methods has been achieved. We found that the PV performance and stability of PSCs fabricated with these films were superior to those with preferred orientation along the (110) plane. In this work, TA was first introduced into the perovskite precursor solutions to stabilize the crystal structure of the Sn−Pb binary perovskite. The reducing and the chelating properties of TA make it perform two functions of regulating crystal growth dynamics and inhibiting the oxidation process of Sn^{2+}. Subsequently, the controllable preferential growth evolution of Sn−Pb binary perovskite films from (110) to (224) planes can be realized by further introducing UST on the corresponding TA-based precursor solutions and regulating the time. Accordingly, we achieved the preferential growth of TA-based Sn−Pb binary perovskite films along the (224) plane when the time of UST reached 15 min, with the highest PCE of 15.59% for the corresponding devices. The improved performance is mainly attributed to the optimized charge transport, enhanced crystallinity, reduced defect states, and so forth. Moreover, the long-term stability can also be improved due to the retarded crystallization rate and oxidation process of Sn^{2+}. Thus, the combination of Lewis base TA and UST is a feasible and simple approach to achieve the preferential growth of the (224) facet. This controllable method for preferential growth of perovskite films was also an effective approach to improve device performance and stability.

■ EXPERIMENTAL SECTION

Materials. Lead iodide (PbI_2, purity >99.9%), stannous iodide (SnI_2, purity >99.99%), cesium iodide (CsI, purity >99.99%), stannous fluoride (SnF_2, purity >99.95%), methylammonium iodide (CH_3NH_3I, purity ≥99.9%), and reagents such as anhydrous *N*,*N*-dimethylformamide (DMF, purity >99.9%), dimethyl sulfoxide (DMSO, purity >99.9%), and chlorobenzene (CB, purity >99.9%) were all purchased from Yingkou You Xuan Trade Co., Ltd. TA (purity >99.5%) was purchased from Sinopharm Chemical Reagent Corporation Co., Ltd., [6,6]-Phenyl-C_{61}-butyric acid methyl ester (PCBM) and poly(3,4-ethylenedioxythiophene) polystyrene sulfonate (PEDOT:PSS) (Clevios P VP AI 4083, Heraeus) were purchased from Xi'an Polymer Light Technology Corp. All solvents were used without further modification and purification.

Solar Cell Fabrication. Indium tin oxide (ITO) transparent electrode substrates (sheet resistance ≈15 Ω sq^{-1} and thickness: 1.1 mm) were ultrasonically cleaned with detergent, deionized water, ethanol, acetone, and isopropanol for 30 min. Subsequently, the substrates prepared for use were dried under a nitrogen flow for a period of time (10−20 s) and dealt with ultraviolet−ozone for 20 min to remove the organic residues from the surface of substrates and to improve the wettability of PEDOT:PSS solutions on them. The PEDOT:PSS solutions were then spin-coated on cleaned ITO substrates at 4000 rpm for 60 s and annealed at 140 °C for 15 min under air atmosphere. The $MAPbI_3$-based perovskite precursor solutions were prepared as follows: MAI powder (174.9 mg) and a slightly excess amount of PbI_2 powder (510.5 mg) were dissolved in DMF (700 μL) and DMSO (300 μL) mixed solvents at a total concentration of 1.1 M. $MASnI_3$- and $CsSnI_3$-based perovskite precursor solutions were also configured in a similar ratio to $MAPbI_3$-based solutions with a total concentration of 1.1 M, except that the solvent mixture was consisted of DMF (800 μL) and DMSO (200 μL). To prepare additive-containing precursor solutions, 10% molar ratio of additives (SnF_2 or TA) were added into the $MASnI_3$- and $CsSnI_3$-based precursor solutions. All solutions were filtered through 0.45 μm PTFE filters prior to use. Subsequently, the precursor solutions of $MAPbI_3$ (750 μL), $MASnI_3$ (150 μL), and $CsSnI_3$ (100 μL) were mixed and stirred at 60 °C for 1 h to prepare the Sn−Pb binary perovskite precursor solutions. The perovskite precursor solutions (85 μL) were then extracted and spin-coated onto PEDOT:PSS layers at 5000 rpm for 30 s in a nitrogen-filled glove box. While 400 μL of CB was dropped onto the substrate for 15 s, the obtained films were then annealed directly at 120 °C for 10 min. When the substrates were cooled to room temperature, we extracted 45 μL of PCBM solutions dissolved in 1,2-dichlorobenzene at a concentration of 20 mg/mL and spin-coated on the perovskite films at 2000 rpm for 30 s. Finally, 150 nm thick Ag was deposited as a back electrode using thermal evaporation under high vacuum ($<6.6 \times 10^{-4}$ Pa).

Characterization. The absorption spectra were recorded in the range of 400−1000 nm using a UV−vis−near-infrared spectrophotometer (UV-3600) equipped with an integrating sphere. X-ray diffraction (XRD) patterns were obtained by a Rigaku D/Max-ga X-ray diffractometer with Cu Kα radiation (λ = 1.5418 Å) at 40 kV and 40 mA. Field emission scanning electron microscopy (SEM) was used to obtain both the top-down and cross-sectional views using a Hitachi S-4800 system at 5 kV. Atomic force microscopy (AFM) measurements were performed by Oxford Instruments (MFP-3D-BIO) equipped with a time-resolved fluorescence confocal microscope. Photoluminescence (PL) spectra were acquired under excitation of a 488 nm continuous wave laser. Fourier transform infrared (FTIR) spectra were obtained by Thermo Fisher (IS50R) in the range of 4000−500 cm^{-1}. High-resolution transmission electron microscopy (HRTEM) imaging was conducted by Oxford Instruments (JEM-2100F) at an accelerating voltage of 200 kV. The 2D grazing incidence X-Ray diffraction (GIXRD) data were measured at the Beijing Synchrotron Radiation Facility 1W1A diffuse X-ray Scattering Station (BSRF-1W1A) using X-ray at a wavelength of 1.54 Å. The patterns were acquired by a MarCCD mounted vertically at 438 mm from the sample with an exposure time of 20 s.

J−*V* characteristic curves were recorded with a Keithley 2400 source meter measurement system equipped with AM1.5G spectra and calibrated with a standard silicon reference cell (91160V Oriel Instruments) to reach an illumination of 1000 W m^{-2}. All devices were characterized by using a non-reflective metal mask with an effective area of 0.1 cm^2, the scan rates were all set to 80 mV s^{-1} in both the forward (from 0 to 0.8 V) and the reverse (from 0.8 to 0 V) directions during the measurement. The incident photon-to-electron conversion efficiency (IPCE) spectra were recorded from the range of 360 to 1000 nm using an IPCE device (QEX10, PV Measurement) with monochromatic light and the photocurrents were measured with a lock-in amplifier. The electrochemical impedance spectroscopy (EIS) was recorded by a Princeton electrochemical workstation (PARSTAT 4000) under dark conditions in the frequency range of 0.1 to 10^5 HZ.

■ RESULTS AND DISCUSSION

All devices were constructed with the inverted structure of ITO/PEDOT:PSS/$MA_{0.9}Cs_{0.1}Pb_{0.75}Sn_{0.25}I_3$/PCBM/Ag to investigate the effects of SnF_2, TA, and the preferred orientation of different crystal planes on perovskite films and device performance. The schematic and energy-level diagrams are shown in Figure 1a,b. To optimize light absorption of perovskite films, we first regulated the optical properties of PEDOT:PSS hole transport layers (HTLs). The corresponding optical transmittance spectra at different annealing temperatures and times are illustrated in Figure S1a,b, respectively. By comparison, we can conclude that the optimal optical transparency of HTLs can be obtained at an annealing temperature of 140 °C for 15 min. We then proceeded to prepare Sn−Pb binary perovskite absorber layers on them using the same spin-coating procedure to further investigate the effects of SnF_2 and TA on their surface morphology and crystal growth. Subsequently, the colors of the control, SnF_2-, and TA-based perovskite precursor solutions were macroscopically compared, while the color variations after exposure to air [50% relative humidity (RH) and 25 °C] for 10 min. As shown in Figure S1c, both SnF_2- and TA-based perovskite precursor solutions were light yellow compared with the dark yellow color of the control counterpart. We deduced that TA can also serve as a reducing function such as SnF_2 and inhibit the oxidation process of Sn^{2+}. Furthermore, Sn^{2+} is easily oxidized to Sn^{4+} when exposed to air, which makes the solution darker in color. The slight changes in the color of the SnF_2- and TA-based solutions compared with that of the control one further confirmed the above analysis as illustrated in Figure S1d. By analyzing the intrinsic properties of SnF_2 and TA, it can be found that the reduction mechanism of TA is different from that of SnF_2 because TA cannot introduce excessive amount of Sn^{2+} to suppress the oxidation of Sn^{2+} as SnF_2 does.[29] However, the hydroxyl groups on TA can be oxidized to aldehydes, ketones, or carboxylic acids, while the above oxidation products have strong reducibility, which can further retard the oxidation process of Sn^{2+} to a certain extent. In addition to the antioxidant properties, the oxygen atoms in the carboxyl groups and the nitrogen atoms in the amino groups can also be chemically bonded with metal ions due to the inclusion of lone pair of electrons.[30] Thus, it is apt to form coordination bonds with Sn^{2+} and Pb^{2+} due to the chelating property of the oxygen atoms on carboxyl groups in TA, which will also inevitably delay the oxidation process of Sn^{2+} in perovskite precursor solutions and optimize the quality of perovskite absorber layers without causing phase separation.

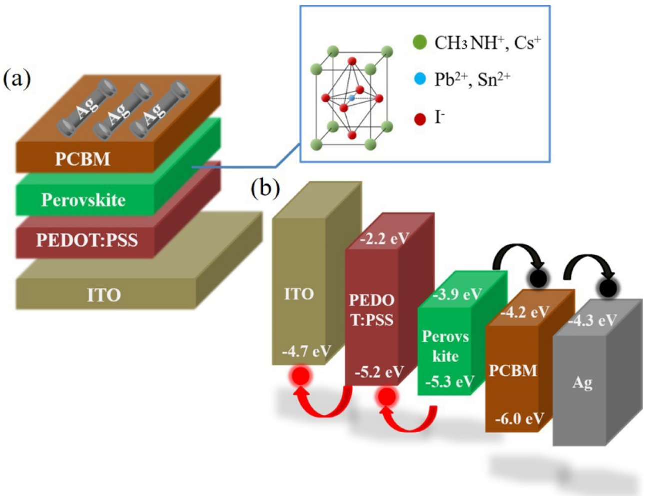

Figure 1. Prepared inverted PSCs for (a) schematic diagram of device configuration. (b) Energy-level alignment diagram.

To explore the effects of SnF_2 and TA on the quality of perovskite films, we compared the top view and cross-sectional SEM images of the perovskite films prepared on ITO/PEDOT:PSS substrates. As shown in Figure 2, the surface morphologies of both control and SnF_2-based films were very poor, while unexpected pinholes were found in these films. The latter significantly degraded the PV performance of devices due to the direct contact between ETLs and HTLs.[31] However, the surface morphology of the TA-based perovskite film was significantly improved as seen from the SEM image in Figure 2g, but the grains on the surface still exhibited irregular distribution. This may be caused by the non-uniform

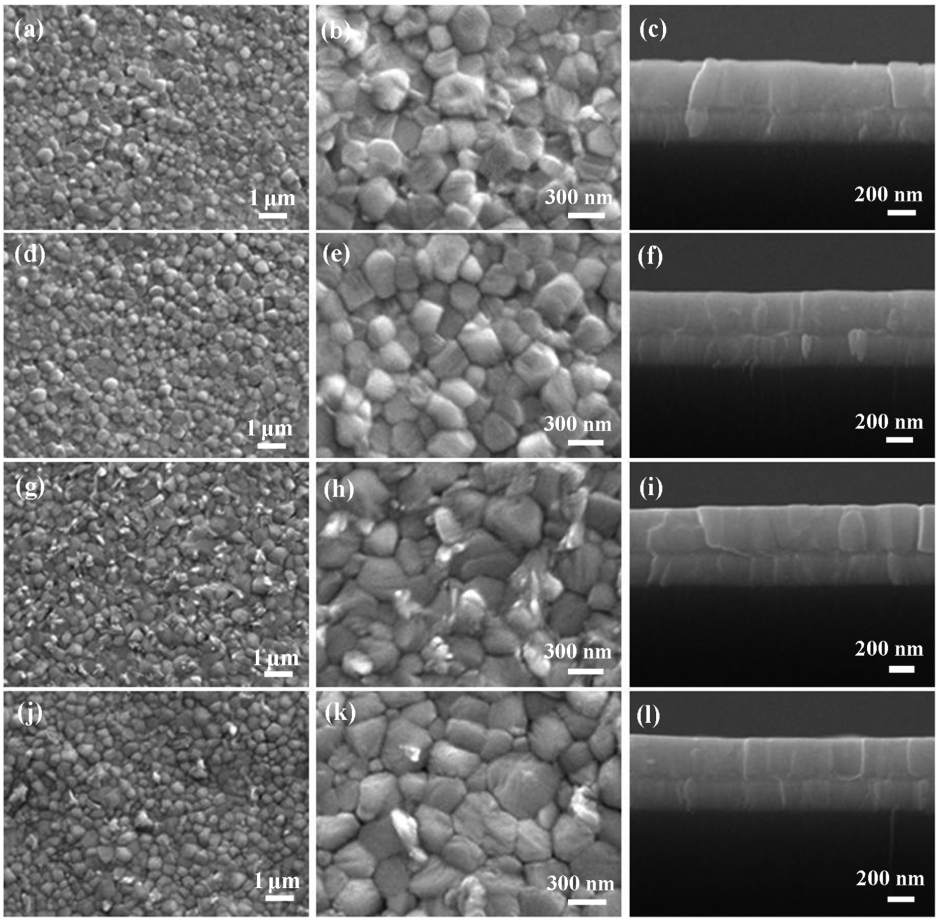

Figure 2. Top-view and cross-sectional SEM images of $MA_{0.9}Cs_{0.1}Pb_{0.75}Sn_{0.25}I_3$ films deposited on PEDOT:PSS substrates prepared from (a−c) control, (d−f) SnF_2-based, (g−i) TA-based, and (j−l) TA-UST-based perovskite precursor solutions.

distribution of TA in perovskite precursor solution and its insufficient chelation with PbI_2 and SnI_2 solutes. To confirm this hypothesis, we then adopted UST on TA-based perovskite precursor solutions to further regulate the crystal growth dynamics and named the samples as TA-UST-based perovskite films. By comparing the two SEM images in Figure 2g,j, we noticed that the quality of the TA-UST-based perovskite film was greatly improved, especially the surface flatness, which can be confirmed by AFM images (Figure S2), wherein the TA-UST-based perovskite film has the smallest root-mean-square surface roughness of 13.7 nm with respect to 14.9, 36.9, and 25.5 nm for the TA-, SnF_2-, and control films, respectively. In addition, by comparing the variations shown in Figure 2b,e,h,k, we noted that the grain size of TA-based perovskite films became larger with or without (w or w/o) UST.

To clarify the reasons for the above differences, we first compared the function of SnF_2 and TA during the growth process of Sn−Pb binary perovskite absorber layers. For the control film, DMSO will be completely volatilized within a few minutes after being extracted by the anti-solvent of CB,[32] leading to the breakage of the intermediate phases of PbI_2/SnI_2·DMSO during annealing at 120 °C and the rapid formation of the crystalline perovskite phase. Such a faster crystallization rate also led to the formation of more pinholes in perovskite films,[33] which is consistent with the poor surface morphology observed in the SEM images of the control film.

As for the SnF_2-based perovskite film, the added SnF_2 will remain in the film during the annealing process because of the high decomposition temperature up to 215 °C. Other studies have shown that the usage of SnF_2 can lead to phase separation in perovskite films, as the addition of SnF_2 into the perovskite precursor solutions disrupted the stoichiometric ratio of the solutes due to the introduction of excess Sn^{2+}. Meanwhile, the large difference in the ionic radii between F^- and I^- led to the fact that F^- cannot be incorporated into the lattice of perovskite crystals, which will not affect the perovskite crystal structure.[34,35] Therefore, SnF_2 only acts as reducing agents and will not be participated in regulating crystal nucleation and the entire growth process of the perovskite crystals, but a large amount of SnF_2 will remain on the grain surface and boundaries as the annealing time increases. We inferred that this is another cause of phase separation in perovskite films, although this phenomenon also favors the passivation of defect states. Thus, both SnF_2-based and control films exhibit similar surface morphology, especially in surface coverage and grain size.

By studying the properties of TA itself, we found that TA also has a high decomposition temperature of about 206 °C, which is similar to that of SnF_2.[36] In addition, the chelating property of TA also gave it the property of Lewis base. According to the Lewis acid−base theory, the formation of intermediate phases and the time of its presence greatly affect the crystallization rate of perovskite films when a one-step anti-solvent method is adopted.[37] The longer the persistence of the intermediate phase, the slower the formation of the perovskite structure, which influences the crystal growth kinetics and the

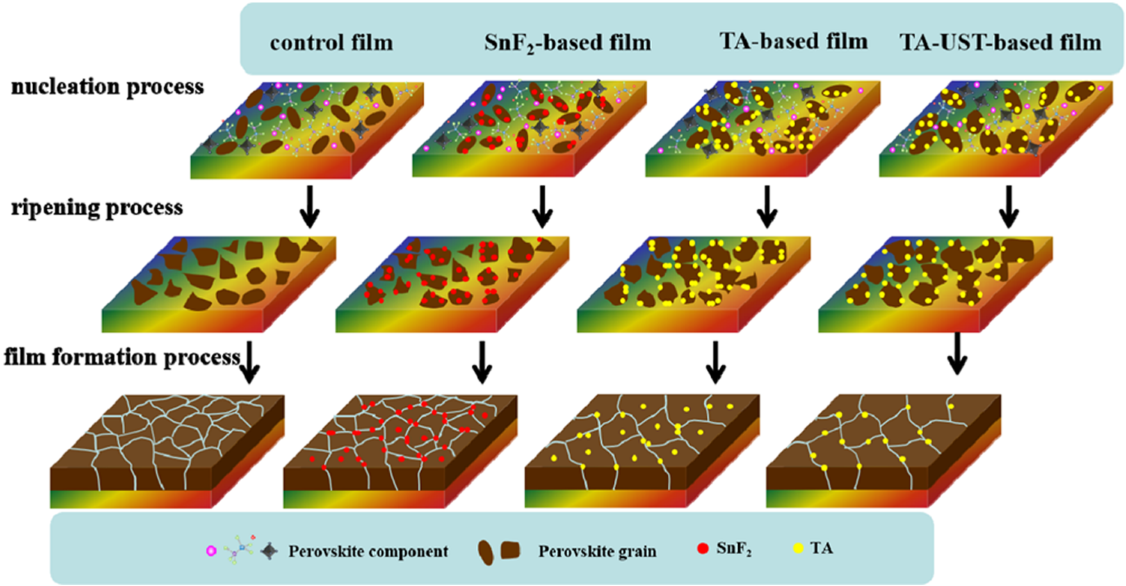

Figure 3. Schematic diagrams of crystal growth kinetics of control, SnF_2-, TA-, and TA-UST-based perovskite films spin-coated on the PEDOT:PSS substrates during different growth processes.

final quality of the perovskite film. The effect of this action can be observed in SEM images, where flatter perovskite films tend to form during the annealing period due to the retarded crystallization rate and the coalescence of small perovskite grains into larger grains.[38] To demonstrate that this law is also valid in our case, we collected the SEM images of perovskite films after annealing for 2 and 6 min. As shown in Figure S3, the morphologies of the four samples were improved and average grain sizes were also increased to some extent with increasing annealing time. In particular, both TA- and TA-UST-based perovskite films exhibit flatter morphologies and larger size at each stage.

Considering the existing theories of grain nucleation and growth in polycrystalline thin films,[39] the crystal growth kinetics can be divided into two processes: nucleation and ripening. For the nucleation process, we learnt that the changes in Gibbs free energy can affect the heterogeneous nucleation of perovskite grains by altering or modifying the charge transport layers and adjusting the chemical state of perovskite precursor solutions, which in turn changes the nucleation number and ultimately affects the growth process of the perovskite grains. However, in our case, we adopted the same chemical materials and procedures to prepare PEDOT:PSS HTMs, which had essentially the same effect on the nucleation of the perovskite films prepared on them, while the one-step spin-coating procedures and anti-solvent technique are also the same for preparing perovskite films. The state of perovskite precursor solutions before and after the introduction of SnF_2 or TA was the only variable that leads to the differences in the perovskite films. As mentioned above, unlike SnF_2, the introduction of TA in perovskite precursor solutions can serve as Lewis bases, which can complex with PbI_2/SnI_2 to form the $PbI_2/SnI_2{\cdot}TA$ intermediate phases. This will form fewer nuclei compared with the control and SnF_2-based counterparts. The growth process of perovskite polycrystals is relatively long compared to the nucleation process. Therefore, we mainly depicted the effects of SnF_2, TA, and UST in perovskite precursor solutions on the growth process of perovskite films in Figure 3 and summarized as follows: initially, island-shaped films were formed on all substrates, but the grains of TA- and TA-UST-based perovskite films were larger than those of control and SnF_2-based ones. As the annealing time increased, all films became more continuous and the perovskite grains gradually became larger. For both the control and SnF_2-based ones, they still exhibited almost identical and smaller grain size compared with their counterparts. Unlike SnF_2, the functional groups in TA determined that it can work as Lewis bases and chelate with Pb^{2+} and Sn^{2+} in perovskite precursor solutions. Meanwhile, TA will interact with the solutes throughout the growth process due to the higher decomposition temperature. According to the above SEM analysis results, the improved surface morphology, enhanced flatness, and increased grain size of perovskite films can be attributed to the retarded crystallization rete and the prolonged ripening process.

To more visually compare the variations of control, SnF_2-, and TA-based perovskite films during the crystallization process, we recorded the color changes of these films at low annealing temperatures of 60 °C for different times from 1 to 15 s. It can be seem from Figure S4, the film formation rate of SnF_2- and TA-based perovskite films is slower than that of the control film because both SnF_2 and TA can retard the oxidation process of Sn^{2+}, thus slowing down the crystallization rate of perovskite crystals to some extent. Moreover, the chelating property of TA can further delay the crystallization rate by forming $PbI_2/SnI_2{\cdot}TA$ intermediate phase due to the same action of TA and DMSO. Subsequently, we prepared DMF (0.5 mM) solutions of PbI_2/SnI_2 and PbI_2/SnI_2 + TA with the same concentrations to validate the presence of the $PbI_2/SnI_2{\cdot}TA$ intermediate phases through a series of characterizations. First, we compared the different states of these precursor solutions by observing the colors of solutions. As illustrated in Figure S5a,b, PbI_2/SnI_2 was initially poorly soluble when stored in DMF solution for 5 min and it was completely dissolved until 1 h. However, it will achieve essentially complete dissolution within 5 min in DMF solution containing TA due to the formation of the $PbI_2/SnI_2{\cdot}TA$ intermediate phases. To further verify the above discussion, we also conducted the ultraviolet−visible (UV−vis) and FTIR

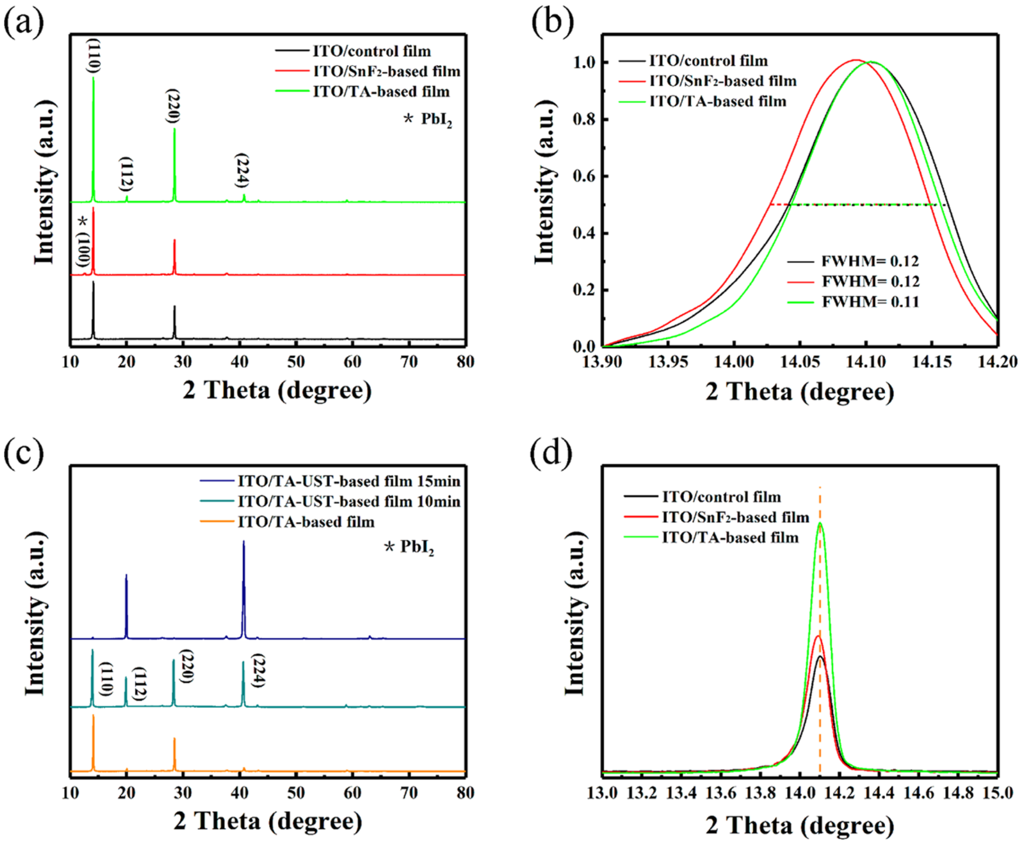

Figure 4. (a) XRD patterns of control, SnF_2-, and TA-based perovskite films. (b) Normalized XRD pattern of (110) peak for control, SnF_2-, and TA-based perovskite films. (c) XRD patterns of TA-UST-based perovskite films with different times of UST. (d) XRD pattern of the (110) plane for control, SnF_2-, and TA-based perovskite films.

spectra measurements. From the UV−vis spectra in Figure S5c, it can be seen that the absorption peak of TA-containing solution was blue-shifted compared with that of TA-free solution, indicating the existence of intermolecular interactions between PbI_2/SnI_2 and TA.[40] Furthermore, from the FTIR spectra in Figure S5d, it can be seen that the C═O (ν(C═O)) stretching vibrations in TA and DMF are at 1733 and 1682 cm^{-1}, respectively.[41,42] It shifted to 1655 cm^{-1} for C═O in DMF for PbI_2/SnI_2-DMF solution due to the formation of the intermediate phase of $PbI_2/SnI_2 \cdot DMF$. Similarly, it shifted to 1715 and 1659 cm^{-1} for C═O in TA and DMF for PbI_2/SnI_2 + TA-DMF solution after the formation of $PbI_2/SnI_2 \cdot TA$ and $PbI_2/SnI_2 \cdot DMF$, respectively. The larger shift of C═O in TA indicated the stronger interaction between PbI_2/SnI_2 and TA than DMF and more favorably indicating the presence of $PbI_2/SnI_2 \cdot TA$ in the precursor solution. However, such small-molecule additive TA with chelating properties would not be uniformly dispersed in the perovskite precursor solutions without the assistance of UST. During the growth process, part of them will accumulate at the grain boundaries, leading to the formation of irregular perovskite grains, as depicted in Figure 2h,i. To avoid this phenomenon, we adopted ultrasonic means to treat TA-based perovskite precursor solutions. The principles of UST were summarized as follows: the adoption of UST can promote a more adequate interaction between PbI_2/SnI_2 and TA in TA-based perovskite precursor solutions, which serves to regulate the state of TA-based perovskite precursor solutions and retard the disordered crystallization. In addition, we have learnt that the coordination interactions are usually directional, so the introduction of chelating agent TA will affect the growth rate and patterns of polycrystalline materials along different crystal planes. Since UST can further modulate the interaction between PbI_2/SnI_2 and TA, the distribution of $PbI_2/SnI_2 \cdot TA$ intermediate phases on the PEDOT:PSS substrates will be more uniform. Meanwhile, the gradual removal of TA during the annealing process of perovskite films can lead to the recrystallization of PbI_2/SnI_2, which eventually also affected the growth patterns of PbI_2/SnI_2 on the substrates.

The cross-sectional SEM images of above samples with ITO/PEDOT:PSS/perovskite/PCBM as the structure are also shown in Figure 2c,f,i,l. We adopted the same preparation processes for each functional layer to avoid its effect on the perovskite films of all samples. Thus, the crystal morphology presented in cross-sectional SEM images mainly reflected the influence of SnF_2 and TA on the preferential orientation growth of perovskite films. We found that the control and SnF_2-based perovskite films showed similar crystal growth trends and did not exhibit significant grain boundaries. However, the preferential orientation growth of perovskite grains became more obvious for TA-based films. In particular, when we adopted UST, distinct grain boundaries and relatively flat interfaces were also observed in the film. On this basis, we argued that TA would play a better role in regulating crystal growth kinetics compared with SnF_2, which greatly affected the morphology, flatness, and crystallinity of perovskite films.

To further reveal the effects of additive modulation on the crystal quality of perovskite films, we compared the XRD patterns of the control, SnF_2-, and TA-based films in Figure 4a. All XRD patterns exhibited two intense diffraction peaks at

14.1 and 28.4°, which corresponded to the (110) and (220) planes, and confirmed the formation of the tetragonal phase perovskite structure.[43] Meanwhile, the intensities of these two diffraction peaks of TA-based film are stronger than those of SnF_2-based and control films, indicating the higher crystal quality of the TA-based film. Two diffraction peaks located at 20.4 and 40.7° were also observed, corresponding to the (112) and (224) planes, respectively. Thus, we can infer that TA in the precursor solution plays a significant role in regulating the crystal structure of the Sn−Pb perovskites.

The initial expected concentration of Sn^{2+} in perovskite precursor solutions for these samples should be the same. However, the introduction of SnF_2 into the precursor solution will inevitably increase the doping concentration of Sn^{2+}. In this case, all the diffraction peaks of SnF_2-based film should shift to higher angles since the radius of Sn^{2+} (1.35 Å) is smaller than that of Pb^{2+} (1.49 Å), which should lead to smaller cell parameters. Moreover, the radius of F^- is smaller than that of I^-, so it does not enter into the lattice of perovskite and will not have any effect on the structure of the lattice. However, in Figure 4b, we found that the (110) and (220) diffraction peaks of SnF_2-based sample were shifted to lower angles than those of TA-based and control samples, while the diffraction peaks associated with the (112) and (224) planes maintained at the same position. According to previous reports, if only some of the diffraction peaks in the XRD pattern were shifted, it should be caused by the residual stress in the film.[44] Thus, the residual stress should be existed in the SnF_2-based perovskite film, which may also be one of the reasons for the poor surface morphology observed in SEM images.

In addition, an extra diffraction peak located at 12.65° was observed in the XRD pattern of the SnF_2-based perovskite film, which corresponded to the impurity phase or unreacted PbI_2/SnI_2.[45,46] This phenomenon could be attributed to the introduction of excess amount of the Sn^{2+} source, which breaks the equimolar equilibrium of the solutes. However, no diffraction peaks of excess PbI_2/SnI_2 were observed in the TA-based perovskite film, which was due to the chelating property of TA that enhanced the solubility of PbI_2/SnI_2 in perovskite precursor solutions and inhibited the formation of Sn^{4+} by forming intermediate phases of $PbI_2/SnI_2{\cdot}TA$. As a result, the TA-based perovskite film exhibited better crystalline quality since their characteristic diffraction peaks were stronger than those in the control and SnF_2-based films. In addition, the full width at half-maximum (fwhm) of (110) diffraction peaks of the above perovskite films was also calculated in Figure 4b to quantify the variation of grain size, wherein the fwhm of both control and SnF_2-based films was 0.12 nm, while the fwhm of TA-based film exhibited a smaller value of 0.11 nm, which further indicated that the usage of TA facilitated the formation of Sn−Pb binary perovskite films with larger grain size and high crystallinity.

To further analyze the effect of UST on crystal structures of perovskite films prepared from control, SnF_2-, and TA-based perovskite precursor solutions, we treated these sealed perovskite precursor solutions with ultrasonication for 10 and 15 min, respectively. As shown in Figures 4c and S6a,b, the preferred orientation growth of perovskite polycrystals of the control and SnF_2-based perovskite films was always along the (110) plane with increasing time of UST, but the intensities of diffraction peaks were enhanced, while the preferred orientation of crystal growth significantly changed with time of UST for TA-based perovskite films. Initially, the diffraction peaks in the (110) and (220) planes exhibited the strongest intensities of the TA-based perovskite film without UST. After the time of UST reached 10 min, the diffraction peaks in the (112) and (224) planes became more pronounced, and the crystal planes in this direction turned into the dominant ones as the time was further increased to 15 min. To analyze the preferred orientation of these perovskite films, the relative intensities of (110), (112), (220), and (224) planes and the ratios of $I_{(224)}/I_{(110)}$ and $I_{(112)}/I_{(220)}$ for all films are summarized in Table S1. Compared with the control film, both SnF_2- and TA-based films exhibited more significant preferred orientation growth in the (110) plane. However, the preferred orientation changed to the (224) plane once the UST time was prolonged to 15 min for the TA-based film. This observation was consistent with the results obtained from cross-sectional SEM images. Generally, the main factors affecting the growth rate of perovskite grains are related to the variations in Gibbs free energy and the components of the absorber layers, including the changes in surface energy and chemical energy.[47,48] In our case, the introduction of TA can further affect the crystal growth dynamics by forming additional $PbI_2/SnI_2{\cdot}TA$ intermediate phases, and this coordination interactions are usually directional, which will reduce the surface energy along the particular crystal planes while changing the growth rate. Let us pay back attention to Table S1, we can find for the TA-based perovskite film, the XRD diffraction peak intensities in the (112) and (224) planes were increased 10 times than those of the control and SnF_2-based films, apart from the enhancement of XRD diffraction peak intensities in the (110) and (220) planes. By carefully analysis, three intermediate phases including $PbI_2/SnI_2{\cdot}TA$, $PbI_2/SnI_2{\cdot}DMF$, and $PbI_2/SnI_2{\cdot}DMSO$ can be formed in TA-based perovskite precursor solutions. We tentatively deduced that the existence of $PbI_2/SnI_2{\cdot}TA$ could enhance the growth rate of perovskite films along the (112) and (224) planes compared with the control and SnF_2-based counterparts since the intermediate phases of $PbI_2/SnI_2{\cdot}DMF$ and $PbI_2/SnI_2{\cdot}DMSO$ could be existed in these three samples. Moreover, the usage of UST resulted in a more uniform dispersion of TA in the perovskite precursor solutions and further promoted the interaction with solutes, making it easier for perovskite grains to grow vertically along the (112) and (224) crystal planes, further promoting the crystallization of the perovskite absorber layers.

Thermal stability is another factor that affected the crystal quality of perovskite films. The measurement technique of obtaining temperature-dependent XRD patterns by slow thermal treatment under low-vacuum conditions can be considered as a means of preparing perovskite films. In this process, the perovskite structure will be formed in a short time because the solvent mixture of DMF and DMSO can be quickly removed under low-vacuum conditions.[49] Therefore, temperature-dependent XRD patterns will directly reflect the effects of SnF_2, TA, and annealing temperatures on the crystal growth, changes in preferential orientation growth, and thermal stability of perovskite films, which can be considered as a unique and effective monitoring technique for characterizing perovskite films. In the discussion section of XRD, we mentioned that the preferential orientation growth along the (224) plane can be fully achieved by adopting UST for 15 min on TA-based perovskite precursor solutions. To investigate whether the process of increasing the temperature gradually

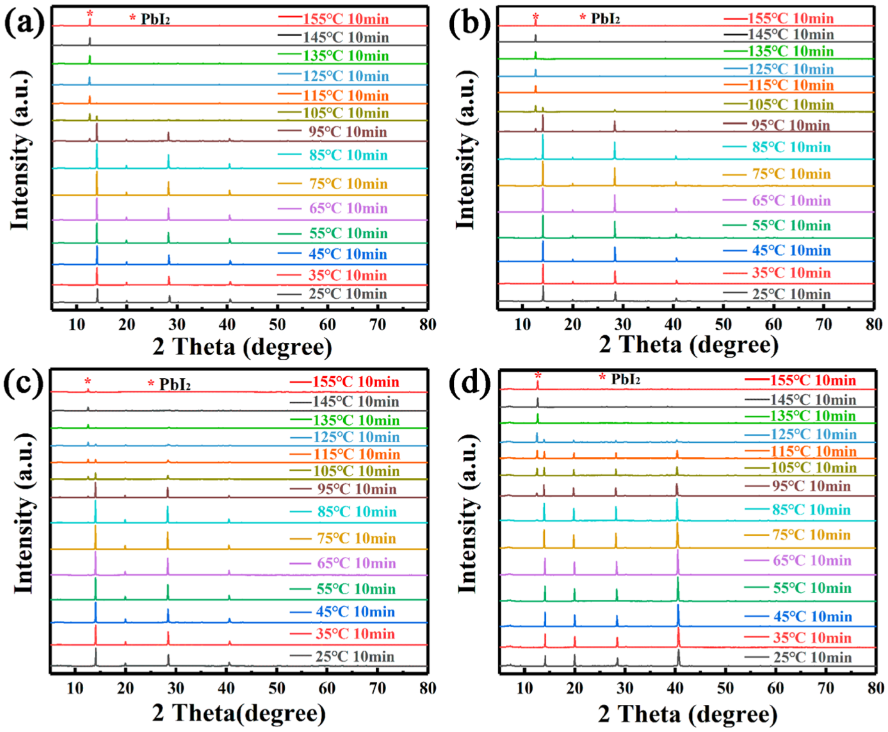

Figure 5. Temperature-dependent XRD patterns of (a) control, (b) SnF_2-, (c) TA-, and (d) TA-UST-based perovskite films.

changed the preferred orientation growth of perovskite films, the perovskite precursor solutions with the UST time of 12 min were selected to prepare TA-UST-based samples and conducted the temperature-dependent XRD measurements, wherein the preferred orientation of perovskite films was in a transition state from (110) to (224) crystal planes. To closely simulate the effect of thermal treatment on perovskite films during the measurements, all perovskite films were synthesized without annealing and only with the anti-solvent treatment. The temperature-dependent XRD measurements were conducted in steps of 2 °C/min over the range of 25−155 °C, and the XRD patterns were examined every 10 °C and waited for 10 min at each temperature point. As shown in Figure 5a−d, we can conclude that the changes in temperature will not alter the original preferred orientation of these formed perovskite films. Moreover, the crystalline quality of all films gradually increased in the range of 25−85 °C, as demonstrated by the increase in the intensity of diffraction peaks. Furthermore, the onset of decomposition of the perovskite films can be inferred from the appearance of the PbI_2/SnI_2 diffraction peak at around 12.65° as the temperature continues to increase beyond 85°. The control and SnF_2-based perovskite films were decomposed completely at around 115 °C, as all characteristic diffraction peaks of the perovskite structure disappeared. However, the complete decomposition temperature of TA-based perovskite films w or w/o UST was extended to 135 °C, indicating that the chelating property of TA can stabilize the structure of the perovskite phase and improve the thermal stability of the perovskite films.

To gain more insights, we investigated the growth trends of diffraction peak intensities in the (110) and (224) planes for all samples with increasing temperature over the whole test range. We set the diffraction intensities at 25 °C as reference values. The intensity ratios of $I_T/I_{T=25}$ as a function of temperature for both (110) and (224) planes in all samples were summarized in Figure S6a. It can be seen that the $I_T/I_{T=25}$ values for both control and SnF_2-based perovskite films increased significantly up to 95 °C, while the growth trend of TA- and TA-UST-based perovskite films was delayed to some extent. The slower growth rates can better regulate the ripening process during the crystal growth kinetics, which further demonstrated that the chelating properties of TA can regulate the growth of polycrystalline perovskite grains.[50,51] With further increase in temperature, the $I_T/I_{T=25}$ values of the latter two samples were significantly larger than those of the former counterparts, indicating the relatively improved thermal stability of TA- and TA-UST-based perovskite films. As shown in Figure S6b, the trends of the diffraction peak intensities of the (224) plane in each sample before 85 °C were almost the same as those of the (110) crystal plane. However, the increase rate of $I_T/I_{T=25}$ in the (224) plane before 85 °C was slower for all perovskite films, especially for that of TA- and TA-UST-based perovskite films, indicating the gradual increase in preferred orientation of TA- and TA-UST-based perovskite films along the (224) crystal plane. In addition, the TA-UST-based films showed some superiority due to the slower reduction rate when the temperature was raised above 95 °C, indicating that the preferential orientation growth along the (224) crystal plane is beneficial for stabilizing the perovskite phase structure. In summary, we showed that the combination of TA and UST was an effective technique to prepare Sn−Pb binary perovskite films with preferred orientation along the (224) crystal plane, superior crystal quality, enlarged grain size, improved surface morphology, enhanced thermal stability, and so forth. To further investigate the effects of enhanced film quality on device performance between 25 and 85 °C, the current density−voltage (J−V) measurements were conducted on 20 devices for each condition, respectively. The statistical distributions of PV parameters including short-circuit current density (J_{SC}), open-circuit voltage (V_{OC}), fill factor (FF), and

PCE are summarized in Figure S7, wherein these PV parameters gradually increased for all devices as the temperature increased from 25 to 85 °C. Moreover, SnF_2-, TA-, and TA-UST-based PSCs exhibited better PV performance compared with the control ones under the same conditions. The stability measurements of devices prepared from the above perovskite films were also investigated using the same conditions as temperature-dependent XRD measurements at 25 °C and 40% RH and were presented in Figure S8, wherein we have restricted the test range from 25 to 115 °C for control and SnF_2-based devices since the perovskite films would be completely decomposed beyond this range and the PCE of PSCs would be zero. Similarly, the test range was from 25 to 135 °C for TA- and TA-UST-based devices. It can be concluded that for the same type of devices, they all exhibited the slow decay rate from 25 to 85 °C due to the progressive increase in crystal quality of perovskite films, but the decay rate will be increased dramatically when exceeding this temperature due of the destruction of the perovskite phase structure. Moreover, the decay rates of SnF_2-, TA-, and TA-UST-based devices sequentially reduced compared with the control devices under the same conditions, indicating the improved crystallinity of perovskite films, which would also enhance the stability of PSCs.

We then utilized the VESTA software to create the perovskite crystals with tetragonal phase structures grown along the (110) and (112) directions, as shown in Figure 6a,b.

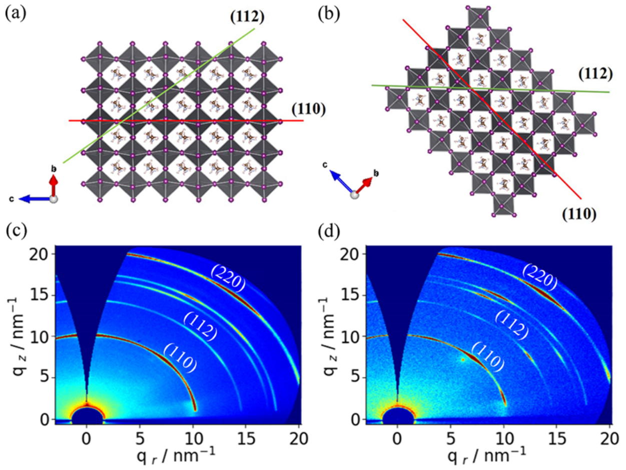

Figure 6. Sn−Pb binary crystal structure with (a) (110) and (b) (112) crystal planes parallel to the substrate. The 2D GIXRD patterns of (c) TA- and (d) TA-UST-based perovskite films.

The different preferred growth orientations were largely determined by the polarity or non-polarity of the exposed surfaces, which significantly influences the optoelectronic properties of polycrystalline perovskite films and corresponding device performance due to the formation of different electronic structures according to Haruyama's work.[52] We have also performed the 2D GIXRD measurements on TA- and TA-UST-based perovskite films, as presented in Figure 6c,d. It can be seen that both figures exhibited similar diffraction patterns, where bright rings or spots can be found around q_r = 10, 14, and 20 nm^{-1}, which corresponded to (110), (112), and (220) crystal planes, respectively. Obviously, both films formed highly textured crystal domains on these substrates. Moreover, we further processed the azimuthally integrated scattering intensity distributions of the diffraction rings or spots along the (110), (112), and (220) crystal planes of these GIXRD patterns, as illustrated in Figure S9. As for radially integrated azimuth intensity plots along the (110) plane, the TA-based perovskite film exhibited a strongest peak at the azimuth angle of 90°. Meanwhile, we can also see other orientation peaks located at the azimuthal angles of 9.8° (180−9.8°), 45.1° (180−45.1°), and 71.6° (180−71.6°). It indicated that the TA-based perovskite films owned multiple ordered crystal orientations, which is beneficial for achieving efficient charge transport within perovskite films. On the contrary, the peak with highest intensity located at 45.1° for the TA-UST-based perovskite film, indicating that the preferred growth orientation of perovskite films had changed from (110) to (112) direction, and a change happened in the main stacking modes of polycrystals compared to the TA-based perovskite film. In addition, all peaks in the plots of TA-UST-based perovskite film also turned sharper, which further proved a significant improvement in crystallinity of the films. Meanwhile, the radially integrated azimuth intensity plots along the (112) plane presented a quite similar variation tendency. Even for the radially integrated azimuth intensity plots along the (220) plane, the peaks in the TA-UST-based film were still sharper than those of the TA-based one. All these results further proved the changed preferred growth orientation and enhanced crystallinity of the TA-UST-based perovskite film, which will be more conducive to efficient charge transport.[53−56]

To further discuss the above preferred orientation growth along (110) and (112) directions, Figure S10 illustrated the HRTEM images and the corresponding selected area electron diffraction images, wherein the region in Figure S10a showed a lattice spacing of 0.32 nm calculated by fast Fourier transform analysis, which corresponded to the (110) plane in TA-based films. Likewise, we can also find a strong signal in the TA-UST-based film with a lattice spacing of 0.22 nm in Figure S10b, corresponding to the (112) crystal plane, which could also indicate the different preferred orientation growth patterns of crystals along (110) and (112) directions in these two films. As shown in Figure S11, X-ray photoelectron spectroscopy (XPS) was also conducted to characterize the chemical ratios of the elements in these perovskite films, where the inset gave the corresponding atomic ratios for each element. It can be derived through calculation that the atomic ratios of I/(Sn + Pb), Cs/(Sn + Pb), and N/(Sn + Pb) for these films were around 3, 0.1, and 1, respectively, which were consistent with the expected ratio for $MA_{0.9}Cs_{0.1}Pb_{0.75}Sn_{0.25}I_3$-based perovskite crystals. Meanwhile, the high-resolution XPS Sn 3d doublets were also shown in Figure S12 to discuss the oxidation problem of Sn^{2+} in these perovskite films. We then further fitted the Sn $3d_{3/2}$ peaks using the Gaussian−Lorentzian functions, and details of the binding energies and the atom ratios of Sn^{2+} and Sn^{4+} are shown in Table S2. It can be seen that the Sn^{4+} signals in SnF_2-, TA-, and TA-UST-based films were much weaker than that in the control film. The strong suppression of Sn^{4+} signals in the XPS spectra of TA- and TA-UST-based films indicated that the introduction of additive TA in perovskite precursor solution showed great potential in suppressing the oxidation of Sn^{2+}. All these will contribute to improve the performance and long-term stability of devices.

The $J-V$ curves for control, SnF_2-, TA-, and TA-UST-based devices are shown in Figure 7a, while the values of PV parameters including J_{SC}, V_{OC}, FF, PCE, series resistance (R_s),

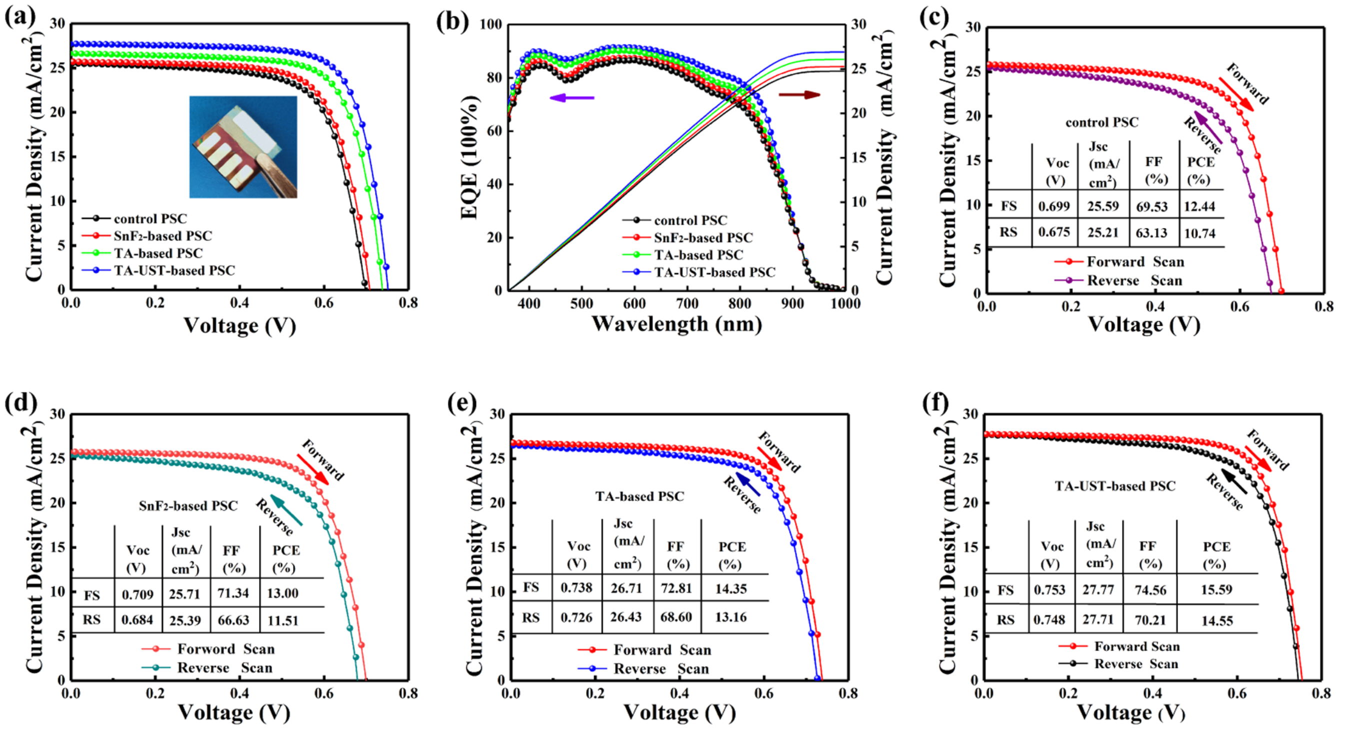

control PSC

	Voc (V)	Jsc (mA/cm^2)	FF (%)	PCE (%)
FS	0.699	25.59	69.53	12.44
RS	0.675	25.21	63.13	10.74

SnF2-based PSC

	Voc (V)	Jsc (mA/cm^2)	FF (%)	PCE (%)
FS	0.709	25.71	71.34	13.00
RS	0.684	25.39	66.63	11.51

TA-based PSC

	Voc (V)	Jsc (mA/cm^2)	FF (%)	PCE (%)
FS	0.738	26.71	72.81	14.35
RS	0.726	26.43	68.60	13.16

TA-UST-based PSC

	Voc (V)	Jsc (mA/cm^2)	FF (%)	PCE (%)
FS	0.753	27.77	74.56	15.59
RS	0.748	27.71	70.21	14.55

Figure 7. (a) *J*−*V* curves of the control, SnF_2-, TA-, and TA-UST-based PSCs measured under the illumination of an AM 1.5 solar simulator (100 mW·cm^{-2}). The scan direction is from open-circuit voltage to short-circuit current (forward). (b) EQE spectra and corresponding integrated J_{sc} of these PSCs. (c−f) The FS and RS curves of these PSCs.

Table 1. PV Parameters of control, SnF_2-, TA-, and TA-UST-Based PSCs

device	V_{oc} (V)	J_{sc} (mA·cm^{-2})	FF (%)	PCE (%)	HI (%)	R_s (Ω·cm^2)	R_{sh} (Ω·cm^2)
control	0.70	25.6	69.5	12.44	15.83	3.25	894.92
SnF_2	0.71	25.7	71.3	13.00	12.95	2.72	1285.58
TA	0.74	26.7	72.8	14.35	9.04	2.68	2102.84
TA-UST	0.75	27.8	74.5	15.59	7.15	2.49	2771.21

and shunt resistance (R_{sh}) are also summarized in Table 1. It can be seen that the performance of devices were gradually improved with the addition of SnF_2, TA, and UST compared with the control one, wherein the increasing trend of J_{sc} exhibited good agreement with integrated J_{sc} from external quantum efficiency (EQE) curves in Figure 7b. The slightly lower integrated J_{sc} values calculated from EQE curves can be attributed to the lower illumination intensity during the EQE acquisition.[57] Moreover, the enhanced J_{sc} can not only be attributed to the gradually improved crystalline quality observed by XRD patterns but also the enhanced light absorption ability, as shown in the UV−vis absorption spectra (Figure 8a), while the increase in grain size also reduced the grain boundaries, which greatly lowered the probability of direct recombination of photogenerated charge carriers, allowing them to be separated more efficiently in the films and thereby enhancing the J_{sc}.[58] The smaller R_s and higher R_{sh} listed in Table 1 further confirm these observations.

To further explore the charge separation, transfer, and extraction properties, the steady-state PL spectra were carried out on perovskite films deposited on soda-lime glass and ITO/PEDOT:PSS substrates, as shown in Figure 8c,d, respectively. As illustrated in Figure 8c, the control, SnF_2-, TA-, and TA-UST-based perovskite films deposited on soda-lime glass exhibited an enhancement trend in PL intensity, which is consistent with the enhanced crystal quality confirmed by XRD. In addition, the blue shift of the PL emission peaks can also be observed in Figure 8c, which is in agreement with the phenomena observed in UV−vis absorption spectra near the band edge region and Tauc curves presented in Figures 8a and S13. Typically, the spontaneous radiative recombination induced by trap states at the perovskite/HTM interface will lead to the red shift of the PL emission peaks.[59] Therefore, it is reasonable to deduce that the effective passivation of these trap states at the surface of the perovskite/HTM or at the perovskite grain boundaries was the main reasons for the blue shift of the PL emission peaks. To reveal the effects of the above improvements on the variations in defect states of the perovskite films, we calculated the Urbach energies from UV−vis absorption spectra of the band edge region as shown in Figure 8b. The formula is described as follows: $\alpha = \alpha_0 \exp(E/E_U)$, where α_0 is a constant, E represents the photon energy at different wavelengths, and E_U is the Urbach energy. The values of E_U for the control, SnF_2-, TA-, and TA-UST-based perovskite films were approximately 195.64, 181.43, 130.75, and 116.47 meV, respectively. Such a significant reduction in E_U values compared with that in the control film implied the lower defect states in perovskite absorber layers, which led to larger blue shifts in the PL emission peak of TA- and TA-UST-based films. In addition, it will also be beneficial for improving the charge transport and extraction properties. As presented in Figure 8d, the gradual quenching of the PL intensities of the

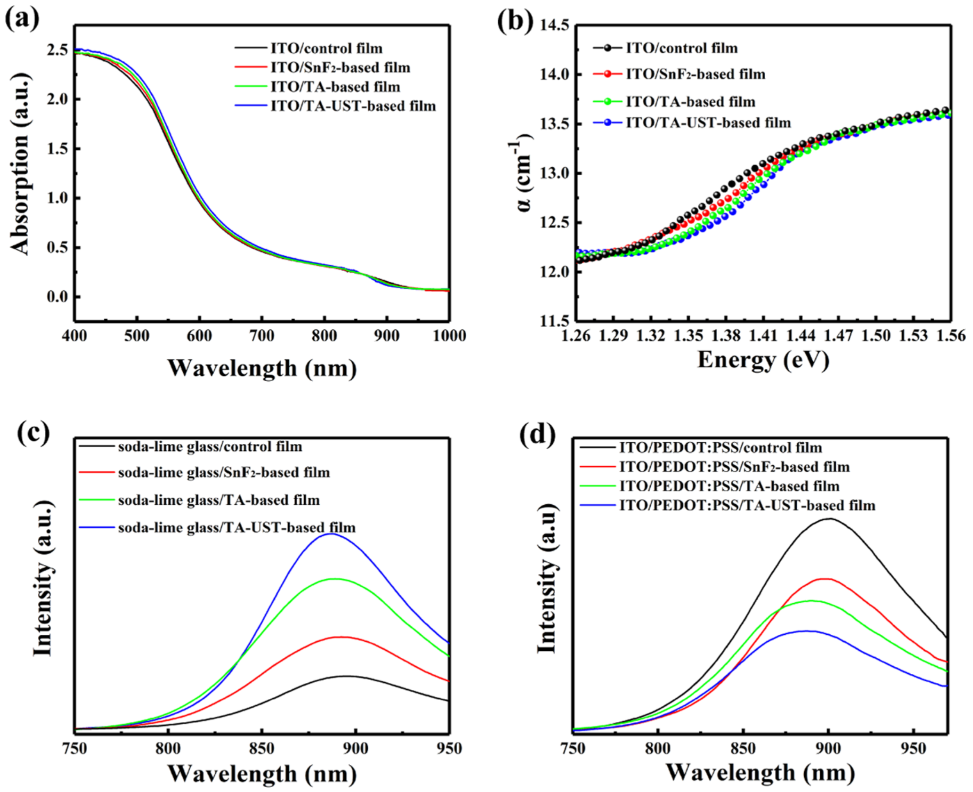

Figure 8. (a) Optical absorption spectra of control, SnF_2-, TA-, and TA-UST-based perovskite films. (b) The Urbach energies corresponding to the value of $\ln(\alpha)$ near the band edge of different films. Steady-state PL spectra deposited on (c) soda-lime glass substrates. (d) ITO/PEDOT:PSS substrates.

control, SnF_2-, TA-, and TA-UST-based perovskite films deposited on the PEDOT:PSS layers can be found, which indicated the rapid extraction of hole carriers from the perovskite layer into the HTM.

To quantitatively probe the charge transport and recombination processes, we conducted the EIS spectra measurements for all the devices (Figure 9). The values of R_s, charge transfer resistance (R_{tr}), and recombination resistance (R_{rec}) in EIS can be obtained by fitting the parameters including R_s, R_{tr}, R_{rec}, charge transfer capacitance (C_{tr}), and recombination capacitance (C_{rec}) in the equivalent circuit.[60] The fitted parameters are summarized in Table S3, wherein the values of R_s were obtained from the real axis intercepts of the whole curve at high frequencies. The radius magnitudes of the high- and low-frequency arcs corresponded to the values of R_{tr} and R_{rec}, respectively. It can be seen that the SnF_2-based device achieved lower values of R_s and R_{tr} but higher R_{rec} compared with those in control devices, and such trends became more pronounced for TA and TA-UST-based devices, which facilitated the charge transport at both HTM/perovskite and perovskite/ETM interfaces and reduced the recombination rate of charge carriers within devices.

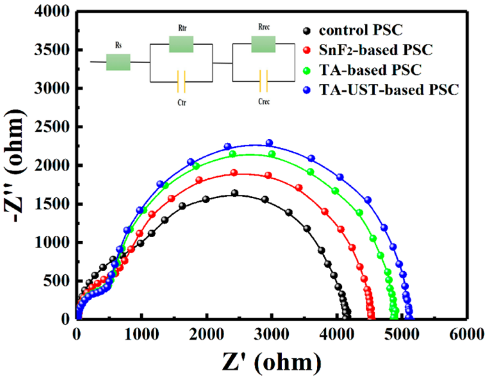

Figure 9. EIS spectra of control, SnF_2-, TA-, and TA-UST-based PSCs measured in dark condition under a 0 V bias voltage. The inset is the equivalent circuit model for the fitting.

The hysteresis phenomenon is also one of the essential factors in characterizing the PV performance of the PSCs. We then presented the PCE values for the forward scan (FS) and reverse scan (RS) curves for control, SnF_2-, TA-, and TA-UST-based PSCs in Figure 7c−f. Since the FS and RS curves do not overlap exactly, all devices suffered varying degrees of hysteresis. For quantitative analysis, the hysteresis index "HI" $\left(\mathrm{HI} = \frac{\mathrm{PCE}_{\mathrm{forward}} - \mathrm{PCE}_{\mathrm{reverse}}}{\mathrm{PCE}_{\mathrm{reverse}}}\right)$ was calculated and the values are summarized in Table 1. The HI values for the control, SnF_2-, TA-, and TA-UST-based PSCs were 15.83, 12.95, 9.04, and 7.15%, respectively. The origin of hysteresis within PV devices is normally attributed to ion migration, the existence of trap states, the accumulation of charge carriers at the interface, and ferroelectric effects within perovskite materials.[61,62] In our case, we inferred that the reduction of HI for SnF_2- and TA-based devices was mainly associated with the reduction in defect-state densities. In addition, for TA-UST-based devices, the chelation between TA and PbI_2/SnI_2 was more adequate, which greatly promoted grain growth and reduced grain boundaries, thus reducing the channels for ion migration, which ultimately led to the more suppressed hysteresis. On the other hand, the improved film quality also increased the reproducibility of devices to some extent, which can be fed back from the histograms of the efficiency distribution in Figure S14a−d. The average PCEs for control, SnF_2-, TA-, and TA-UST-based PSCs were 11.5 ± 0.5, 12.0 ± 0.5, 13.5 ± 0.5, and 14.5 ± 0.5%, respectively.

We also performed water contact angle measurements to investigate the moisture stability of these Sn−Pb binary perovskite films. As presented in Figure S15, the water contact angles on the control, SnF_2-, TA-, and TA-UST-based films increased from 55.5 to 60.1, 63.2, and 66.7°, respectively, demonstrating the enhanced moisture stability of TA- and TA-UST-based films.[63,64] Moreover, the long-term stability and thermal stability of these PSCs were also investigated. Accordingly, the decay curves of the PCE under ambient conditions at 25 °C and 40% humidity are shown in Figure S16a. It can be seen from Figure S16a that SnF_2-, TA-, and TA-UST-based devices can still maintain 83, 85, and 86% of the initial values after 1 month of storage, which was superior to that of control device (71%). Likewise, in Figure S16b, when heated at 85 °C for 200 h, the control device retained only 46.5% of its initial PCE value, which was lower than that of 52.9, 55.5, and 58.4% of SnF_2-, TA-, and TA-UST-based counterparts, respectively. Therefore, we further verified the great improvement in the thermal stability of these modified devices. Normally, grain boundaries are considered to be the main pathways for moisture to penetrate into the interior of the perovskite lattice.[65,66] Therefore, we deduced that the progressively improved surface morphology, enhanced crystalline quality, reduced defect states, and enlarged grain size were responsible for the improved chemical and moisture stability of the PSCs in our case.

■ CONCLUSIONS

In summary, we have developed an effective method to achieve controlled preferential orientation growth of Sn−Pb binary polycrystalline perovskite films along the (224) plane. The combination of TA and UST techniques has proven to be an effective method to achieve the preferential orientation of the (224) crystal plane due to the effective modulation of additional intermediates of $PbI_2/SnI_2{\cdot}TA$. Such changes in crystal growth orientation has been well demonstrated from the above XRD and GIXRD plots. We inferred that the introduction of Lewis bases of TA in perovskite precursor solutions can greatly promote the anisotropic growth of grains along the (224) plane. To better exploit the chelating property of TA, with the assistance of ultrasonic external forces, we found that the preferential orientation growth of Sn−Pb binary perovskite films along the (110) or (224) planes could be achieved by adjusting the time of UST without changing the amount of TA. As a result, perovskite films with enhanced crystallinity, reduced roughness, and defect states can be achieved, which greatly facilitated the charge transport within perovskite films. Meanwhile, the enlarged grain size and reduced trap-state densities also suppressed the hysteresis and enhanced the chemical and water stability of the PSCs. Therefore, regulating the state of perovskite precursor solutions also contributed to improved device performance. Our work described a way to fabricate high-quality Sn−Pb binary perovskite films using a simple and effective method with preferred orientation along the (224) plane. This approach was also promising for stabilizing other low-toxic binary perovskite films and realizing the preferential orientation growth of perovskite polycrystalline films.

■ ASSOCIATED CONTENT

Supporting Information

The Supporting Information is available free of charge at https://pubs.acs.org/doi/10.1021/acsami.0c19014.

> More details on the characterization of experimental results, optical transmittance spectra, photographs of perovskite precursor solutions, AFM images, SEM images, photographs of perovskite films, images of solution states, UV−vis absorption spectra, FTIR spectra, XRD patterns, statistical distribution of device performance, stability test, radially integrated azimuth intensity plots, HRTEM images, XPS and HRXPS spectra, Tauc curves, histogram of PCE distributions, water contract angles, and long-term stability measurements (PDF)

■ AUTHOR INFORMATION

Corresponding Authors

Jinghai Yang − *Key Laboratory of Functional Materials Physics and Chemistry of the Ministry of Education, Jilin Normal University, Changchun 130103, P.R. China;* orcid.org/0000-0001-8409-6035; Email: jhyang1@jlnu.edu.cn

Lili Yang − *Key Laboratory of Functional Materials Physics and Chemistry of the Ministry of Education, Jilin Normal University, Changchun 130103, P.R. China; National Demonstration Center for Experimental Physics Education, Jilin Normal University, Siping 136000, P.R. China;* orcid.org/0000-0003-0333-1684; Email: llyang1980@126.com

Federico Rosei − *Key Laboratory of Functional Materials Physics and Chemistry of the Ministry of Education, Jilin Normal University, Changchun 130103, P.R. China; Centre Énergie, Materiaux et Télécommunications, Institut National de la Recherche Scientifique, Varennes, Québec J3X 1S2, Canada;* orcid.org/0000-0001-8479-6955; Email: rosei@emt.inrs.ca

Authors

Yansen Sun − *Changchun Institute of Optics, Fine Mechanics and Physics, Chinese Academy of Sciences, Changchun 130033, P.R. China; University of Chinese Academy of Sciences, Beijing 100049, P.R. China*

Shuo Yang − *Changchun Institute of Optics, Fine Mechanics and Physics, Chinese Academy of Sciences, Changchun 130033, P.R. China*

Zhenyu Pang − *Changchun Institute of Optics, Fine Mechanics and Physics, Chinese Academy of Sciences, Changchun 130033, P.R. China; University of Chinese Academy of Sciences, Beijing 100049, P.R. China*

Yingnan Quan − *Key Laboratory of Functional Materials Physics and Chemistry of the Ministry of Education, Jilin Normal University, Changchun 130103, P.R. China*

Rongfei Song − *National Demonstration Center for Experimental Physics Education, Jilin Normal University, Siping 136000, P.R. China*

Yu Chen − *Institute of High Energy Physics, Chinese Academy of Sciences, Beijing 100049, P.R. China*

Weiheng Qi − *Institute of High Energy Physics, Chinese Academy of Sciences, Beijing 100049, P.R. China*
Yanbo Gao − *Key Laboratory of Functional Materials Physics and Chemistry of the Ministry of Education, Jilin Normal University, Changchun 130103, P.R. China*
Fengyou Wang − *Key Laboratory of Functional Materials Physics and Chemistry of the Ministry of Education, Jilin Normal University, Changchun 130103, P.R. China; National Demonstration Center for Experimental Physics Education, Jilin Normal University, Siping 136000, P.R. China*
Xinyuan Zhang − *Changchun Institute of Optics, Fine Mechanics and Physics, Chinese Academy of Sciences, Changchun 130033, P.R. China; University of Chinese Academy of Sciences, Beijing 100049, P.R. China*
Yunfei Sun − *Key Laboratory of Functional Materials Physics and Chemistry of the Ministry of Education, Jilin Normal University, Changchun 130103, P.R. China*

Complete contact information is available at:
https://pubs.acs.org/10.1021/acsami.0c19014

Notes

The authors declare no competing financial interest.

■ ACKNOWLEDGMENTS

The authors would like to acknowledge the financial support for this work from the National Nature Science Foundation of China (grant nos. 61775081, 22075101, 11904127, and 61475063), Program for the development of Science and Technology of Jilin province (item nos. 20200801032GH, 20190103002JH, 20190103039JH, and 20180414008GH), the Thirteenth Five-Year Program for Science and Technology of Education Department of Jilin Province (item nos. JJKH20190998KJ, JJKH20190994KJ, JJKH20191021KJ, JJKH20191022KJ, and JJKH20191019KJ), and Construction Program for Innovation Research Team of Jilin Normal University (grant no. 201703). F. Rosei is grateful to the Canada Research Chairs program for partial salary support. A portion of this work is based on the data obtained at BSRF-1W1A. The authors gratefully acknowledge the cooperation of Y. Chen and W. Qi at the BSRF-1W1A beamline.

■ REFERENCES

(1) Yang, W. S.; Noh, J. H.; Jeon, N. J.; Kim, Y. C.; Ryu, S.; Seo, J.; Seok, S. I. High-performance Photovoltaic Perovskite Layers Fabricated through Intramolecular Exchange. *Science* **2015**, *348*, 1234−1237.

(2) Eperon, G. E.; Burlakov, V. M.; Docampo, P.; Goriely, A.; Snaith, H. J. Morphological Control for High Performance, Solution-Processed Planar Heterojunction Perovskite Solar Cells. *Adv. Funct. Mater.* **2013**, *24*, 151−157.

(3) National Renewable Energy Laboratory (NREL) Best Research-Cell Efficiency Chart. https://www.nrel.gov/pv/cell-efficiency.html (accessed August, 2020).

(4) Wang, F.; Yang, M.; Zhang, Y.; Yang, L.; Fan, L.; Lv, S.; Liu, X.; Han, D.; Yang, J. Activating Old Materials with New Architecture: Boosting Performance of Perovskite Solar Cells with H_2O-Assisted Hierarchical Electron Transporting Layers. *Adv. Sci.* **2019**, *6*, 1801170.

(5) Kim, Y.-H.; Cho, H.; Heo, J. H.; Kim, T.-S.; Myoung, N.; Lee, C.-L.; Im, S. H.; Lee, T.-W. Multicolored Organic/Inorganic Hybrid Perovskite Light-Emitting Diodes. *Adv. Mater.* **2015**, *27*, 1248−1254.

(6) Fang, H.-H.; Wang, F.; Adjokatse, S.; Zhao, N.; Even, J.; Loi, M. A. Photoexcitation Dynamics in Solution-Processed Formamidinium Lead Iodide Perovskite Thin Films for Solar Cell Applications. *Light Sci. Appl.* **2016**, *5*, No. e16056.

(7) Kim, H.-S.; Lee, C.-R.; Im, J.-H.; Lee, K.-B.; Moehl, T.; Marchioro, A.; Moon, S.-J.; Humphry-Baker, R.; Yum, J.-H.; Moser, J. E.; Grätzel, M.; Park, N.-G. Lead Iodide Perovskite Sensitized All-Solid-State Submicron Thin Film Mesoscopic Solar Cell with Efficiency Exceeding 9%. *Sci. Rep.* **2012**, *2*, 591.

(8) Krishna, A.; Gottis, S.; Nazeeruddin, M. K.; Sauvage, F. Mixed Dimensional 2D/3D Hybrid Perovskite Absorbers: The Future of Perovskite Solar Cells? *Adv. Funct. Mater.* **2019**, *29*, 1806482.

(9) Hu, W.; Zhou, W.; Lei, X.; Zhou, P.; Zhang, M.; Chen, T.; Zeng, H.; Zhu, J.; Dai, S.; Yang, S.; Yang, S. Low-Temperature In Situ Amino Functionalization of TiO_2 Nanoparticles Sharpens Electron Management Achieving over 21% Efficient Planar Perovskite Solar Cells. *Adv. Mater.* **2019**, *8*, 1806095.

(10) Leblebici, S. Y.; Linn, L.; Li, Y. B.; Reyes-Lillo, S. E.; Wickenburg, S.; Wong, E.; Lee, J.; Melli, M.; Ziegler, D.; Angell, D. K.; Ogletree, D. F.; Ashby, P. D.; Toma, F. M.; Neaton, J. B.; Sharp, I. D.; Weber-Bargioni, A. Facet-Dependent Photovoltaic Efficiency Variations in Single Grains of Hybrid Halide Perovskite. *Nat. Energy* **2016**, *1*, 16093.

(11) de Quilettes, D. W.; Vorpahl, S. M.; Stranks, S. D.; Nagaoka, H.; Eperon, G. E.; Ziffer, M. E.; Snaith, H. J.; Ginger, D. S. Impact of Microstructure on Local Carrier Lifetime in Perovskite Solar Cells. *Science* **2015**, *348*, 683−686.

(12) Zheng, G.; Zhu, C.; Ma, J.; Zhang, X.; Tang, G.; Li, R.; Chen, Y.; Li, L.; Hu, J.; Hong, J.; Chen, Q.; Gao, X.; Zhou, H. Manipulation of Facet Orientation in Hybrid Perovskite Polycrystalline Films by Cation Cascade. *Nat. Commun.* **2018**, *9*, 2793.

(13) Liu, L.; Tang, Z.; Xin, C.; Zhu, S.; An, S.; Wang, N.; Fan, L.; Wei, C.; Huang, Q.; Hou, G.; Zhao, Y.; Ding, Y.; Zhang, X. Acetate Anion Assisted Crystal Orientation Reconstruction in Organic−Inorganic Lead Halide Perovskite. *ACS Appl. Energy Mater.* **2018**, *1*, 2730−2739.

(14) Cho, N.; Li, F.; Turedi, B.; Sinatra, L.; Sarmah, S. P.; Parida, M. R.; Saidaminov, M. I.; Murali, B.; Burlakov, V. M.; Goriely, A.; Mohammed, O. F.; Wu, T.; Bakr, O. M. Pure Crystal Orientation and Anisotropic Charge Transport in Large-Area Hybrid Perovskite Films. *Nat. Commun.* **2016**, *7*, 13407.

(15) Li, W.; Fan, J.; Mai, Y.; Wang, L. Aquointermediate Assisted Highly Orientated Perovskite Thin Films toward Thermally Stable and Efficient Solar Cells. *Adv. Energy Mater.* **2017**, *7*, 1601433.

(16) Wang, F.; Zhang, Y.; Yang, M.; Fan, L.; Yang, L.; Sui, Y.; Yang, J.; Zhang, X. Toward Ultra-Thin and Omnidirectional Perovskite Solar Cells: Concurrent Improvement in Conversion Efficiency by Employing Light-Trapping and Recrystallizing Treatment. *Nano Energy* **2019**, *60*, 198−204.

(17) Wang, Z.; Shi, Z.; Li, T.; Chen, Y.; Huang, W. Stability of Perovskite Solar Cells: A Prospective on the Substitution of the A Cation and X Anion. *Angew. Chem., Int. Ed.* **2017**, *56*, 1190−1212.

(18) Babayigit, A.; Ethirajan, A.; Muller, M.; Conings, B. Toxicity of Organometal Halide Perovskite Solar Cells. *Nat. Mater.* **2016**, *15*, 247−251.

(19) Gu, L.; Fan, Z. Perovskite/Organic-Semiconductor Heterojunctions for Ultrasensitive Photodetection. *Light Sci. Appl.* **2017**, *6*, No. e17090.

(20) Liao, W.; Zhao, D.; Yu, Y.; Shrestha, N.; Ghimire, K.; Grice, C. R.; Wang, C.; Xiao, Y.; Cimaroli, A. J.; Ellingson, R. J.; Podraza, N. J.; Zhu, K.; Xiong, R.-G.; Yan, Y. Fabrication of Efficient Low-Bandgap Perovskite Solar Cells by Combining Formamidinium Tin Iodide with Methylammonium Lead Iodide. *J. Am. Chem. Soc.* **2016**, *138*, 12360−12363.

(21) Kapil, G.; Ripolles, T. S.; Hamada, K.; Ogomi, Y.; Bessho, T.; Kinoshita, T.; Chantana, J.; Yoshino, K.; Shen, Q.; Toyoda, T.; Minemoto, T.; Murakami, T. N.; Segawa, H.; Hayase, S. Highly Efficient 17.6% Tin−Lead Mixed Perovskite Solar Cells Realized through Spike Structure. *Nano Lett.* **2018**, *18*, 3600−3607.

(22) Zhang, J.; Wu, S.; Liu, T.; Zhu, Z.; Jen, A. K. Y. Boosting Photovoltaic Performance for Lead Halide Perovskites Solar Cells with BF_4^- Anion Substitutions. *Adv. Funct. Mater.* **2019**, *29*, 1808833.

(23) Ge, X.; Qu, X.; He, L.; Sun, Y.; Guan, X.; Pang, Z.; Wang, C.; Yang, L.; Wang, F.; Rosei, F. 3D Low Toxicity Cu−Pb Binary Perovskite Films and their Photoluminescent/Photovoltaic Performance. *J. Mater. Chem. A* **2019**, *7*, 27225−27235.

(24) Hao, F.; Stoumpos, C. C.; Chang, R. P. H.; Kanatzidis, M. G. Anomalous Band Gap Behavior in Mixed Sn and Pb Perovskites Enables Broadening of Absorption Spectrum in Solar Cells. *J. Am. Chem. Soc.* **2014**, *136*, 8094−8099.

(25) Anaya, M.; Correa-Baena, J. P.; Lozano, G.; Saliba, M.; Anguita, P.; Roose, B.; Abate, A.; Steiner, U.; Grätzel, M.; Calvo, M. E.; Hagfeldt, A.; Míguez, H. Optical Analysis of $CH_3NH_3Sn_xPb_{1-x}I_3$ Absorbers: a Roadmap for Perovskite-on-Perovskite Tandem Solar Cells. *J. Mater. Chem. A* **2016**, *4*, 11214−11221.

(26) Hirsekorn, S. The Scattering of Ultrasonic Waves by Polycrystals. *J. Acoust. Soc. Am.* **1982**, *72*, 1021−1031.

(27) Gielen, B.; Jordens, J.; Thomassen, L.; Braeken, L.; Van Gerven, T. Agglomeration Control during Ultrasonic Crystallization of an Active Pharmaceutical Ingredient. *Crystals* **2017**, *7*, 40.

(28) Kamat, P. V.; Bisquert, J.; Buriak, J. Lead-Free Perovskite Solar Cells. *ACS Energy Lett.* **2017**, *2*, 904−905.

(29) Li, Z.; Klein, T. R.; Kim, D. H.; Yang, M.; Berry, J. J.; van Hest, M. F. A. M.; Zhu, K. Scalable Fabrication of Perovskite Solar Cells. *Nat. Rev. Mater.* **2018**, 3, 18017.

(30) Kim, W.; Jung, M. S.; Lee, S.; Choi, Y. J.; Kim, J. K.; Chai, S. U.; Kim, W.; Choi, D.-G.; Ahn, H.; Cho, J. H.; Choi, D.; Shin, H.; Kim, D.; Park, J. H. Oriented Grains with Preferred Low-Angle Grain Boundaries in Halide Perovskite Films by Pressure-Induced Crystallization. *Adv. Energy Mater.* **2017**, *8*, 1702369.

(31) Liao, W.; Zhao, D.; Yu, Y.; Grice, C. R.; Wang, C.; Cimaroli, A. J.; Schulz, P.; Meng, W.; Zhu, K.; Xiong, R.; Yan, Y. Lead-Free Inverted Planar Formamidinium Tin Triiodide Perovskite Solar Cells Achieving Power Conversion Efficiencies up to 6.22%. *Adv. Mater.* **2016**, *28*, 9333−9340.

(32) Silverman, D. C.; Kalota, D. J.; Stover, F. S. Effect of pH on Corrosion Inhibition of Steel by Polyaspartic Acid. *Corros. Sci.* **1995**, *51*, 818−825.

(33) Ye, S.; Rao, H.; Zhao, Z.; Zhang, L.; Bao, H.; Sun, W.; Li, Y.; Gu, F.; Wang, J.; Liu, Z.; Bian, Z.; Huang, C. A Breakthrough Efficiency of 19.9% Obtained in Inverted Perovskite Solar Cells by Using an Efficient Trap State Passivator Cu(thiourea)I. *J. Am. Chem. Soc.* **2017**, *139*, 7504−7512.

(34) Gupta, S.; Cahen, D.; Hodes, G. How SnF_2 Impacts the Material Properties of Lead-Free Tin Perovskites. *J. Phys. Chem. C* **2018**, *122*, 13926−13936.

(35) Kumar, M. H.; Dharani, S.; Leong, W. L.; Boix, P. P.; Prabhakar, R. R.; Baikie, T.; Shi, C.; Ding, H.; Ramesh, R.; Asta, M.; Graetzel, M.; Mhaisalkar, S. G.; Mathews, N. Lead-Free Halide Perovskite Solar Cells with High Photocurrents Realized Through Vacancy Modulation. *Adv. Mater.* **2014**, *26*, 7122−7127.

(36) Sun, Y.; Pang, Z.; Quan, Y.; Han, D.; Zhang, X.; Ge, X.; Wang, F.; Sun, Y.; Yang, J.; Yang, L. A Synchronous Defect Passivation Strategy for Constructing High-Performance and Stable Planar Perovskite Solar Cells. *Chem. Eng. J.* **2020**, 127387.

(37) Azmi, R.; Hadmojo, W. T.; Sinaga, S.; Lee, C.-L.; Yoon, S. C.; Jung, I. H.; Jang, S.-Y. Perovskite Solar Cells: High-Efficiency Low-Temperature ZnO Based Perovskite Solar Cells Based on Highly Polar, Nonwetting Self-Assembled Molecular Layers. *Adv. Energy Mater.* **2018**, *8*, 1701683.

(38) Burschka, J.; Pellet, N.; Moon, S.-J.; Humphry-Baker, R.; Gao, P.; Nazeeruddin, M. K.; Grätzel, M. Sequential Deposition as a Route to High-Performance Perovskite-Sensitized Solar Cells. *Nature* **2013**, *499*, 316−319.

(39) Ahn, N.; Son, D. Y.; Jang, I. H.; Kang, S. M.; Choi, M.; Park, N. G. Highly Reproducible Perovskite Solar Cells with Average Efficiency of 18.3% and Best Efficiency of 19.7% Fabricated via Lewis Base Adduct of Lead(II) Iodide. *J. Am. Chem. Soc.* **2015**, *137*, 8696−8699.

(40) Reddy, S. S.; Arivunithi, V. M.; Sree, V. G.; Kwon, H.; Park, J.; Kang, Y.-C.; Zhu, H.; Noh, Y.-Y.; Jin, S.-H. Lewis Acid-Base Adduct-Type Organic Hole Transport Material for High Performance and Air-Stable Perovskite Solar Cells. *Nano Energy* **2019**, *58*, 284−292.

(41) Lee, S.; Tang, M.-C.; Munir, R.; Barrit, D.; Kim, Y.-J.; Kang, R.; Yun, J.-M.; Smilgies, D.-M.; Amassian, A.; Kim, D.-Y. In Situ Study of Film Formation Mechanism of Organic-Inorganic Hybrid Perovskite Solar Cells: Controlling the Solvate Phase by Additive System. *J. Mater. Chem. A* **2020**, *8*, 7695−7703.

(42) Fahmi, M. Z.; Wathoniyyah, M.; Khasanah, M.; Rahardjo, Y.; Wafiroh, S.; Abdulloh, A. Ncorporation of Graphene Oxide in Polyethersulfone Mixed Matrix Membranes to Enhance Hemodialysis Membrane Performance. *RSC Adv.* **2018**, *8*, 931−937.

(43) Zhu, L.; Xu, Y.; Zhang, P.; Shi, J.; Zhao, Y.; Zhang, H.; Wu, J.; Luo, Y.; Li, D.; Meng, Q. Investigation on the Role of Lewis Bases in the Ripening Process of Perovskite Films for Highly Efficient Perovskite Solar Cells. *J. Mater. Chem. A* **2017**, *5*, 20874−20881.

(44) Zhao, H.; Wang, S.; Sun, M.; Zhang, F.; Li, X.; Xiao, Y. Enhanced Stability and Optoelectronic Properties of $MAPbI_3$ Films by a Cationic Surface-Active Agent for Perovskite Solar Cells. *J. Mater. Chem. A* **2018**, *6*, 10825−10834.

(45) Hu, W.; Cong, H.; Huang, W.; Huang, Y.; Chen, L.; Pan, A.; Xue, C. Germanium/Perovskite Heterostructure for High-Performance and Broadband Photodetector from Visible to Infrared Telecommunication Band. *Light Sci. Appl.* **2019**, *8*, 106.

(46) Noyan, I. C.; Huang, T. C.; York, B. R. Residual Stress/Strain Analysis in Thin Films by X-ray Diffraction. *Crit. Rev. Solid State Mater. Sci.* **1995**, *20*, 125−177.

(47) Li, Y.; Sun, W.; Yan, W.; Ye, S.; Rao, H.; Peng, H.; Zhao, Z.; Bian, Z.; Liu, Z.; Zhou, H.; Huang, C. 50% Sn-Based Planar Perovskite Solar Cell with Power Conversion Efficiency up to 13.6%. *Adv. Energy Mater.* **2016**, *6*, 1601353.

(48) Watthage, S. C.; Song, Z.; Shrestha, N.; Phillips, A. B.; Liyanage, G. K.; Roland, P. J.; Ellingson, R. J.; Heben, M. J. Enhanced Grain Size, Photoluminescence, and Photoconversion Efficiency with Cadmium Addition during the Two-Step Growth of $CH_3NH_3PbI_3$. *ACS Appl. Mater. Interfaces* **2017**, *9*, 2334−2341.

(49) Thompson, C. V.; Carel, R. Stress and Grain Growth in Thin Films. *J. Mech. Phys. Solid.* **1996**, *44*, 657−673.

(50) Thompson, C. V. Structure Evolution during Processing of Polycrystalline Films. *Annu. Rev. Mater. Sci.* **2000**, *30*, 159−190.

(51) Yang, L.; Gao, Y.; Wu, Y.; Xue, X.; Wang, F.; Sui, Y.; Sun, Y.; Wei, M.; Liu, X.; Liu, H. Novel Insight into the Role of Chlorobenzene Antisolvent Engineering for Highly Efficient Perovskite Solar Cells: Gradient Diluted Chlorine Doping. *ACS Appl. Mater. Interfaces* **2019**, *11*, 792−801.

(52) Haruyama, J.; Sodeyama, K.; Han, L.; Tateyama, Y. Termination Dependence of Tetragonal $CH_3NH_3PbI_3$ Surfaces for Perovskite Solar Cells. *J. Phys. Chem. Lett.* **2014**, *5*, 2903−2909.

(53) Wehrenfennig, C.; Eperon, G. E.; Johnston, M. B.; Snaith, H. J.; Herz, L. M. High Charge Carrier Mobilities and Lifetimes in Organolead Trihalide Perovskites. *Adv. Mater.* **2014**, *26*, 1584−1589.

(54) Wang, Z.-K.; Li, M.; Yang, Y.-G.; Hu, Y.; Ma, H.; Gao, X.-Y.; Liao, L.-S. High Efficiency Pb−In Binary Metal Perovskite Solar Cells. *Adv. Mater.* **2016**, *28*, 6767.

(55) Xu, Z.; Liu, Z.; Li, N.; Tang, G.; Zheng, G.; Zhu, C.; Chen, Y.; Wang, L.; Huang, Y.; Li, L.; Zhou, N.; Hong, J.; Chen, Q.; Zhou, H. A Thermodynamically Favored Crystal Orientation in Mixed Formamidinium/Methylammonium Perovskite for Efficient Solar Cells. *Adv. Mater.* **2019**, *31*, 1900390.

(56) Li, M.; Wang, Z.-K.; Zhuo, M.-P.; Hu, Y.; Hu, K.-H.; Ye, Q.-Q.; Jain, S. M.; Yang, Y.-G.; Gao, X.-Y.; Liao, L.-S. Pb−Sn−Cu Ternary Organometallic Halide Perovskite Solar Cells. *Adv. Mater.* **2018**, *30*, 1800258.

(57) Pang, Z.; Sun, Y.; Gao, Y.; Zhang, X.; Sun, Y.; Yang, J.; Wang, F.; Yang, L. Unravelling the Mechanism of Interface Passivation

Engineering for Achieving High-Efficient ZnO-Based Planar Perovskite Solar Cells. *J. Power Sources* **2019**, *438*, 226957.

(58) Liang, P.-W.; Chueh, C.-C.; Xin, X.-K.; Zuo, F.; Williams, S. T.; Liao, C.-Y.; Jen, A. K.-Y. High-Performance Planar-Heterojunction Solar Cells Based on Ternary Halide Large-Band-Gap Perovskites. *Adv. Energy Mater.* **2015**, *5*, 1400960.

(59) Yang, D.; Zhou, X.; Yang, R.; Yang, Z.; Yu, W.; Wang, X.; Li, C.; Liu, S.; Chang, R. P. H. Surface Optimization to Eliminate Hysteresis for Record Efficiency Planar Perovskite Solar Cells. *Energy Environ. Sci.* **2016**, *9*, 3071−3078.

(60) Yu, Z.; Zhang, L.; Tian, S.; Zhang, F.; Zhang, B.; Niu, F.; Zeng, P.; Qu, J.; Rudd, P. N.; Huang, J.; Lian, J. Hot-Substrate Deposition of Hole- and Electron-Transport Layers for Enhanced Performance in Perovskite Solar Cells. *Adv. Energy Mater.* **2018**, *8*, 1870007.

(61) Liang, P.-W.; Liao, C.-Y.; Chueh, C.-C.; Zuo, F.; Williams, S. T.; Xin, X.-K.; Lin, J.; Jen, A. K.-Y. Additive Enhanced Crystallization of Solution-Processed Perovskite for Highly Efficient Planar-Heterojunction Solar Cells. *Adv. Mater.* **2014**, *26*, 3748−3754.

(62) Wang, R.; Mujahid, M.; Duan, Y.; Wang, Z. K.; Xue, J.; Yang, Y. A Review of Perovskites Solar Cell Stability. *Adv. Funct. Mater.* **2019**, *29*, 1808843.

(63) Zhao, H.; Han, Y.; Xu, Z.; Duan, C.; Yang, S.; Yuan, S.; Yang, Z.; Liu, Z.; Liu, S. A Novel Anion Doping for Stable $CsPbI_2Br$ Perovskite Solar Cells with an Efficiency of 15.56% and an Open Circuit Voltage of 1.30 V. *Adv. Energy Mater.* **2019**, *9*, 1902279.

(64) Yuan, S.; Qian, F.; Yang, S.; Cai, Y.; Wang, Q.; Sun, J.; Liu, Z.; Liu, S. NbF_5: A Novel α-Phase Stabilizer for FA-Based Perovskite Solar Cells with High Efficiency. *Adv. Funct. Mater.* **2019**, *29*, 1807850.

(65) van Reenen, S.; Kemerink, M.; Snaith, H. J. Modeling Anomalous Hysteresis in Perovskite Solar Cells. *J. Phys. Chem. Lett.* **2015**, *6*, 3808−3814.

(66) Liao, Y.; Liu, H.; Zhou, W.; Yang, D.; Shang, Y.; Shi, Z.; Li, B.; Jiang, X.; Zhang, L.; Quan, L. N.; Quintero-Bermudez, R.; Sutherland, B. R.; Mi, Q.; Sargent, E. H.; Ning, Z. Highly Oriented Low-Dimensional Tin Halide Perovskites with Enhanced Stability and Photovoltaic Performance. *J. Am. Chem. Soc.* **2017**, *139*, 6693−6699.